TISSUE ENGINEERING: Part C
Volume 19, Number 6, 2013

DOI: 10.1089/ten.tec.2012.0007

Dual Contrast Agent for Computed Tomography and Magnetic Resonance Hard Tissue Imaging

Manuela Ventura, MSc,[1,*] Yi Sun, MSc,[2,3,*] Viorel Rusu, PhD,[4] Peter Laverman, PhD,[5] Paul Borm, PhD,[6] Arend Heerschap, PhD,[2] Egbert Oosterwijk, PhD,[3] Otto C. Boerman, PhD,[5] John A. Jansen, DDS, PhD,[1] and X. Frank Walboomers, PhD[1]

Calcium phosphate cements (CPCs) are commonly used bone substitute materials, which closely resemble the composition of the mineral phase of bone. However, this high similarity to natural bone also results in difficult discrimination from the bone tissue by common imaging modalities, that is, plain X-ray radiography and three-dimensional computed tomography (CT). In addition, new imaging techniques introduced for bone tissue visualization, like magnetic resonance imaging (MRI), face a similar problem. Even at high MRI resolution, the lack of contrast between CPCs and surrounding bone is evident. Therefore, this study aimed to evaluate the feasibility of a dual contrast agent, traceable with both CT and MRI as enhancers of CPC/bone tissue contrast. Our formulation is based on the use of silica beads as vectors, which encapsulate and carry contrast-enhancing nanoparticles, in our case, colloidal Gold and Superparamagnetic Iron oxide particles (SPIO). The bead suspension was incorporated within a calcium phosphate powder. The resultant cements were then tested both *in vitro* and *in vivo* in a femoral condyle defect model in rats. Results showed that the mechanical properties of the cement were not significantly affected by the inclusion of the beads. Both *in vitro* and *in vivo* data proved the homogeneous incorporation of the contrast within the cement and its visual localization, characterized by a short-term CT contrast enhancement and a long-term MR effect recognizable by the characteristic blooming shape. Finally, no signs of adverse tissue reactions were noticed *in vivo*. In conclusion, this study proved the feasibility of a multimodal contrast agent as an inert and biocompatible enhancer of CaP cement versus bone tissue contrast.

Introduction

The increasing incidence of bone treatment procedures keeps a high pressure on the development and optimization of substitutes for bone regeneration.[1] Several synthetic bone substitutes are currently available, organic, inorganic, polymer, or ceramic-based materials. Among those, calcium phosphate cements (CPCs) represent a category that closely resembles the structure and composition of natural bone. The excellent biocompatibility of CPC and osteoconductive properties can be further enhanced by the introduction of structural macroporosity, for example, by incorporation of microparticles. The (pre)clinical application of such cements has been demonstrated *in vivo*, for example, in a rat skull augmentation model,[2] alveolar bone regeneration model in beagle dogs,[3] maxillary sinus floor augmentation in sheep,[4] and a critical-sized cranial defect model in rats.[5] Despite their wide use and characterization, less achievements have been reported in the field of *in vivo* visualization and follow-up methods. Plain radiography (X-rays) and computed tomography (CT) are the most employed techniques. On the other hand, recent developments in the field of magnetic resonance imaging (MRI) open the way to a completely new scenario of high-resolution bone visualization applications.[6–8]

A common problem of all imaging modalities remains the high similarity between CPCs and the mineral phase of the bone, which makes it difficult, if not impossible, to clearly discriminate the materials.[9] Several opacifiers have already been proposed to enhance the contrast of CPCs for CT (i.e., barium sulfate, tantalum oxide) and MRI (Iron Oxide Particles, gadolinium).[10–12] As a negative side effect, all the above-mentioned compounds have shown to interact with CPCs, negatively affecting both physical and mechanical properties, even at very low concentrations.[13] Moreover, a major drawback for their *in vivo* application arises from the lack of information regarding behavior and metabolic

Departments of [1]Biomaterials, [2]Radiology, and [3]Urology, Radboud University Nijmegen Medical Center, Nijmegen, The Netherlands.
[4]MagnaMedics Diagnostics BV, Geleen, The Netherlands.
[5]Department of Nuclear Medicine, Radboud University Nijmegen Medical Center, Nijmegen, The Netherlands.
[6]Nano4Imaging, Center for Biomedical Technique, Aachen, Germany.
*These two authors equally contributed to the study.

destiny of heavy metal compounds following the degradation of the CPC material.[14,15]

In this study, we have developed a new nanocomposite that is a silica-based, dual-contrast agent (DCA), detectable with both CT and MRI. The specific formulation of such beads, combined with the chemical inertness and biocompatibility of silica, should allow the maintainance of the positive visualization effects of the selected contrast agents (colloidal gold and SPIO), while at the same time reducing unspecific reactivity, inflammatory tissue reactions, and alteration of the physicomechanical properties of the CPC. Colloidal gold and iron oxide nanoparticles were selected as embedded agents for, respectively, CT and MR imaging, as both compounds are widely characterized and approved for clinical use.[16,17] After *in vitro* characterization, the developed contrast agent was tested *in vivo*, in a femoral condyle defect model in rats. Effects were monitored by scanning the same animals with both CT and MRI up to 8 weeks postsurgery. Finally, histology was performed to prove the biocompatibility of the product.

Materials and Methods

Implant materials

CaP cement. CPC consisted of 85% of α-Tricalcium Phosphate, 10% Dicalcium Phosphate Dihydrate, and 5% Hydroxy Apatite. The cement powder was sterilized using gamma radiation with 25 kGy (Isotron B.V., Ede, The Netherlands).

PLGA microspheres. Poly (DL-Lactic-co-glycolic acid), (PURASORB; Purac, Gorinchem, The Netherlands) with a Lactic to Glycolic acid ratio of 50:50 and an average molecular weight of 4.55 ± 0.03 kDa, was used for microparticle preparation. Acid terminated PLGA microparticles were prepared using a double-emulsion solvent-extraction technique. The average size of the microparticles, as determined with image analysis, was 20 ± 18 μm.[18] PLGA microparticles were mixed with the CaP cement powder in a proportion of 20%wt/wt.

Contrast agent. A customized DCA was synthetized (Nano4Imaging GmbH, Aachen, Germany). The DCA particles were based on an inverse emulsion approach (patent WO2005/052581) using passive MRI responsive SPIO nanoparticles with a mean size of 200 nm and gold nanoparticles of 4 nm as embedded within a silica matrix at an end concentration of 40 wt/wt%. The wt% ratio between SPIO and gold nanoparticles was set at 4:1. The silica carrier particles containing the embedded iron oxide and gold nanoparticles had a mean size of 1.2 μm. They were sealed with an additional layer of silica synthesized using a modified Stoeber method[19] and dried by dry-freezing. The obtained solid phase of DCA particles was then mixed with the hydroxyapatite to reach a final end concentration of 5% (wt/wt) within the bone cement composition.

Composite preparation. The cement was created by adding a filtered sterilized (0.2-μm filter) 2% aqueous solution of sodium phosphate (Na2HPO4) to the PLGA/CaP or PLGA/CaP/DCA powder mixture using a 2-mL syringe (BD Plastipak, Becton Dickinson S.A., Madrid, Spain) with a closed tip. The components were shaken for 20 s using a mixing apparatus (Silamat Vivadent, Schaan, Liechtenstein).

CaP cement/DCA characterization. To ensure proper handling properties of the cement, the following parameters were assessed:

Gillmore test: Initial and final setting times for the different cement formulations were assessed using custom-available Gillmore needles (ASTM C266). A plastic mould of 3 mm (diameter) × 6 mm (height) was used to prepare scaffolds. At least four samples from each formulation were mixed and injected into the mould and both initial and final setting times were determined. Tests were performed at room temperature.

Compression Test: Samples were placed in a testing bench (858 MiniBionixII®; MTS, Eden Prairie, MN) and compressive strength in the longitudinal direction (parallel to the long axis) of the specimens was measured at 0.5 mm/min cross-head speed.

Morphology: The morphology of different cement formulations was determined by scanning electron microscopy (SEM). For this purpose, destructed samples were obtained from the compression test. Images from each sample were obtained at 100×, 500×, and 1000× magnification.

In vitro *assays*

Bone blocks. Bone blocks of $\sim 1.5\,cm^3$ were obtained from fresh pig bone. A 3-mm (depth and diameter) cylindrical defect was drilled using a dental bur and dental drills. The defects were (1) left unfilled, (2) filled with CaP/PLGA cement, and (3) filled with CaP/PLGA cement mixed with 5% of DCA. All samples were then scanned with both micro X-ray computed tomography (μCT) and MR modalities.

In vitro micro-CT. Before scanning, all specimens were dehydrated in ethanol 70% and wrapped in Parafilm® (SERVA Electrophoresis GmbH, Heidelberg, Germany) to prevent the occurrence of drying artifacts during scanning. For three-dimensional (3D) analysis, the specimens were placed vertically onto the sample holder of a micro-CT imaging system (Skyscan 1072, Kontich, Belgium). Subsequently, samples were recorded at a 14.16-μm resolution (X-ray Source 100 kV/98 μA; Magnification 20×; Exposure Time 3.9 s; 1-mm filter applied). Then, using NRecon V1.4 (SkyScan), a cone beam reconstruction was performed on the projected files. Reconstructed files were analyzed using CTAnalyser software (Version 1.10.1.0; SkyScan). Finally, 3D-reconstructions of the samples were also obtained (3D-DOCTOR 4.0, Able Software Corp., Lexington, MA).

In vitro MRI. All samples were embedded in 70% ethanol and MR imaging of bone samples was performed on a 11.7T MR system (Biospec, Bruker, Germany) with a mouse brain surface coil. Zero Echo Time (ZTE) images were acquired at 200 kHz bandwidth, TR = 4 ms, flip angle = 5°, FOV = 50 × 50 × 50 mm, matrix size 128 × 128 × 128, total acquisition time 3.27 min.

In vivo *assays*

Animal model. All *in vivo* work was conducted in accordance with standards and protocols of the Radboud

University Nijmegen Medical Center, Nijmegen, The Netherlands. National guidelines for care and use of laboratory animals were obeyed and approval of the Experimental Animal Ethics Committee was obtained (RU-DEC 2010-225). Eight healthy adult male Wistar rats, weighing 250–300 g were included as experimental animals. Surgery was performed under general inhalation anesthesia (Isoflurane) and aseptic conditions. For the surgical procedure (Fig. 1), animals were immobilized and both legs were shaved, washed, and disinfected. The knee joint was exposed after a longitudinal parapatellar incision. At the femural intercondylar notch, a cylindrical defect (3.0 mm depth and diameter) was then prepared using a dental bur and continuous external cooling with saline. Defects were filled with the CPC material, or left untreated in control animals (Table 1), before the subcutaneous tissue and skin were closed by suturing in layers. *In vivo* CT and MRI scans were performed during time, up to 8 weeks postsurgery. Thereafter, animals were sacrificed and histology and micro-CT were performed.

In vivo CT. Animals were scanned after surgery and at 4 as well as 8 weeks after surgery, using a small animal CT scanner (Inveon; Siemens Preclinical Solutions, Knoxville, TN). Acquisitions were performed under general inhalation anesthesia (Isoflurane). Animals were placed in a supine position in the scanner and images were acquired over ~6 min (spatial resolution 30 μm, 80 kV, 500 μA, exposure time 1000 ms, frame average by 1). Projected files were then reconstructed using a cone beam algorithm.

In vivo MRI. MR imaging was performed the day of the surgery and at 4 as well as 8 weeks after surgery using a 11.7T MR system (Biospec, Bruker, Germany) with a home-built bare Helmholtz coil with a size of 3 × 3 cm. ZTE imaging was performed at 200 kHz bandwidth, TE/TR = 0 ms/8 ms, flip angle = 5°, FOV = 50 × 50 × 50 mm, matrix size:128 × 128 × 128, four averages, and a final acquisition time of 30.27 min.

Micro-CT. Eight weeks after surgery, the animals were sacrificed by CO_2/O_2 overdose. Femoral condyles were retrieved and surrounding soft tissue was removed. Bone samples were fixed in 10% formalin for 48 h and subsequently transferred to 70% ethanol for the duration of the μCT scans. For 3D analysis, the specimens were placed vertically onto the sample holder of a micro-CT imaging system (Skyscan 1072). Subsequently, samples were recorded at a 15.30 μm resolution (X-ray Source 100 kV/98 μA; Exposure Time 3.9 s; 1-mm filter applied). Then, using NRecon V1.4 (SkyScan), a cone beam reconstruction was performed on the projected files. Finally, 3D reconstructions of the samples were obtained (3D-DOCTOR 4.0; Able Software Corp.).

Histology. After scanning, all specimens were decalcified in 5% formic acid at 37°C for 5 days with a daily solution replacement. Samples were then dehydrated in gradual series of ethanol (70%–100%) and embedded in paraffin. Sections of 6 μm thickness were cut in a plane parallel to the long axis of the femur using a Leica RM2165 Microtome (Leica Microsystems, Rijswijk, The Netherlands). The sections were stained with Hematoxylin/Eosin and trichrome

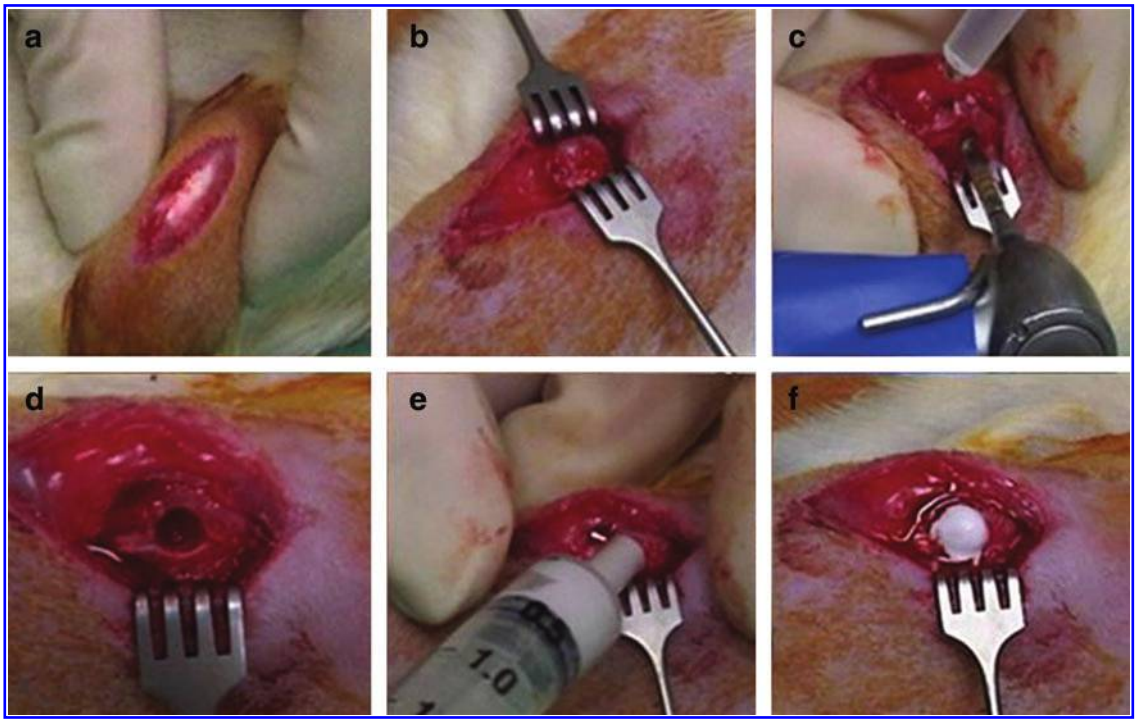

FIG. 1. Surgical procedure of a femoral condyle defect in rats. The knee joint was exposed after a longitudinal parapatellar incision **(a, b)**. At the femural intercondylar notch, a cylindrical defect (3.0 mm depth and diameter) was then prepared using a dental bur and continuous external cooling with saline **(c, d)**. Defects were filled with the calcium phosphate cement (CPC) material **(e, f)**, or left untreated in control animals (Table 1), before the subcutaneous tissue and skin were closed by suturing in layers. Color images available online at www.liebertpub.com/tec

Table 1. Experimental Groups and Implantation Scheme

Rat	*Left*	*Right*
1	No defect	Empty defect
2	Empty defect	CPC
3	CPC	CPC/DCA
4	CPC/DCA	No defect
5	No defect	Empty defect
6	Empty defect	CPC
7	CPC	CPC/DCA
8	CPC/DCA	No defect

CPC, calcium phosphate cement; DCA, dual contrast agent.

Elastin van Gieson (EVG); at least three sections of each specimen were analyzed.

Bone quantification. EVG-stained slides were quantitatively scored using computer-based image analysis techniques (Leica Qwin Pro-image; Leica, Wetzlar, Germany). From digitalized images (magnification 5×), the percentage of bone tissue was determined within the area of interest, positioned between the growth plates, and the cortical bone layer.

Statistical analysis. Statistical analysis for bone quantification was performed using SPSS, version 16.0 (SPSS, Inc., Chicago, IL). Statistical comparisons were performed by one-way analysis of variance (ANOVA) with a Tukey's multiple comparison post-test. For setting time and compression tests, data are presented as mean ± standard deviation and significant differences were determined by ANOVA. Gray values distributions were validated by the Wilcoxon matched-pairs signed-ranks test. Calculations were performed using GraphPad Instat® (GraphPad Software, San Diego, CA). All differences were considered significant at p-values < 0.05.

Results

Initial observations

After freeze-drying, increasing concentrations of DCA, ranging from 1 to 10% (wt/wt%) were incorporated within the CaP/PLGA powder. The lowest concentration required for imaging was reached at 5%. At higher concentrations, the physicomechanical properties of the material were altered. Consequently, 5% was maintained throughout (data not shown).

CaP cement/DCA characterization

To exclude eventual interactions between the DCA and CaP/PLGA matrix, physicomechanical as well as morphological tests were performed. Figure 2a shows the initial and final setting times of the two cements, with and without DCA. The Gillmore test showed no significant differences between the two groups. Initial setting time required around 9 min, while for the final setting time, 21–22 min were needed. The contrast was uniformly mixed with the cement powder, providing a uniform light brown color.

Measurements of the peak load (compression strength) and E-Modulus for CPC, with and without a contrast agent,

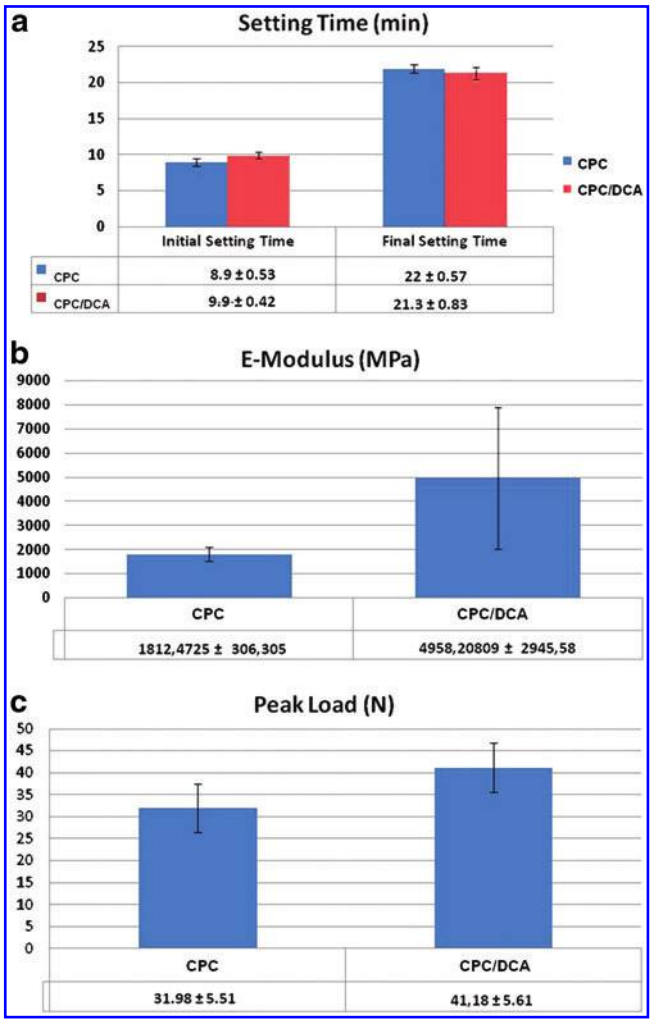

FIG. 2. Mechanical properties of CPC versus CPC/dual contrast agent (DCA). **(a)** Gillmore test for initial and final setting time measurements.; for both composites, initial setting time required 8–9 min, while for the final setting time 21–22 min was required, **(b, c)** respectively, show E-Modulus and Peak Load as measures of the mechanical strength of the two materials. All data are showed as mean value ± standard deviation. Color images available online at www.liebertpub.com/tec

are presented in Figure 2b and 2c, respectively. Both parameters appear slightly altered by the incorporation of the contrast agent, namely, the strength of the resulting material is increased, even though the difference cannot be considered statistically significant.

From the morphological point-of-view, Figure 3 shows representative scanning electron micrographs of CPC and CPC plus the DCA. In both samples, PLGA particles were easily recognizable, dispersed evenly in the Calcium Phosphate matrix. The overall structure appeared uniform between the samples and the presence of the contrast agent did not affect the internal structure of the cement upon visual inspection.

In vitro *assays*

At visual inspection, no differences emerged during both preparation and injection of the cements, with and without

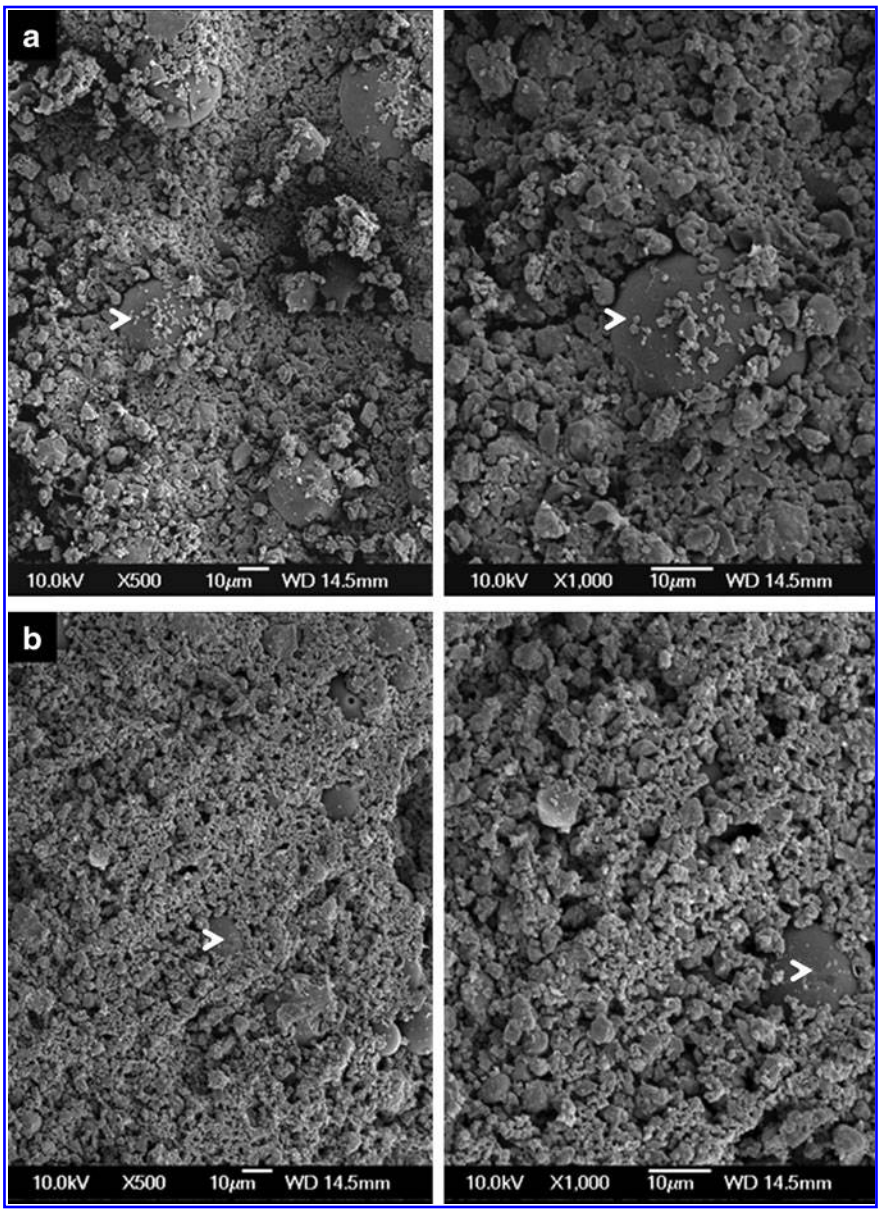

FIG. 3. Scanning electron micrographs. **(a)** CPC containing PLGA microsphere at 500× and 1000× magnification; **(b)** CPC containing PLGA microspheres and DCA at 500× and 1000× magnification. Arrows indicate PLGA microspheres.

5% wt/wt contrast, into the premade bone blocks. After final setting, all samples were scanned with both MRI and μCT.

Magnetic resonance imaging. After mixing with the DCA, the cement was immediately injected to fill the defects created into the cortical layer of the bone blocks (Fig. 4a).

While the untreated defect was easily identifiable in the upper part of the specimen, within the cortical layer (Fig. 4b), in case of defect filled with plain CPC, the visual inspection did not allow localization of the defect area within the surrounding cortical bone (Fig. 4d).

When the DCA was added to the cement, the presence of SPIO particles made the defect easily identifiable as well as characterized by the presence of an artifact known as the blooming effect (result of the dipolar behavior of the iron particles). Although the defect area was easy to localize, the blooming artifact caused an overestimation of the defect size, complicating possible quantification methods (Fig. 4e).

Computed tomography. Based on the images, it was already possible to visually identify a clear difference between plain CPC and CPC with the DCA. Plain CPC could not be discerned from the surrounding cortical bone (Fig. 5a), while with the contrast (Fig. 5b), the difference between the material and bone was evident. Figure 5c shows the unfilled defect as control. The contrast agent was distributed evenly through the cement matrix. Quantitatively, the analysis of gray values revealed two different curves for CPC and CPC/DCA. The curve generated from the empty defect is also included. As shown in Figure 5d, plain CPC gave a distribution peak corresponding to gray values of 100–120. The incorporation of the DCA caused a shift of the population to the left part of the scale, toward gray values ranging from 80 to 90. No peak was found in the empty defect.

In vivo

Animal model. The surgical procedure (Fig. 1) did not lead to any adverse and unexpected reactions. All animals

recovered within a few hours postsurgery and none were restricted in their movements. Rats were monitored during the whole experimental period and no evident signs of discomfort or weight loss were observed. Based on *in vitro* explorative data, the concentration of the DCA to be mixed with the cement powder was set at 5% wt/wt. After 8 weeks, all femoral condyles were retrieved; at macroscopical inspection, no clear differences were detectable between the different groups.

Magnetic resonance imaging. In line with *in vitro* results, injected plain CPC were not detectable in the femoral condyles at any time point and the resulting images were comparable to those obtained from untreated femoral condyles' defects. In contrast, the visibility of the CPC was enhanced by the presence of DCA (Fig. 6) at all evaluation times. The addition of DCA caused a similar blooming effect as in the *in vitro* assay. However, it was observed that visibility and contrast clearly decreased with the increasing implantation time.

Computed tomography. Figure 7 shows that, in agreement with *in vitro* data, no differences in terms of gray values were measured between plain CPC and surrounding bone tissue at any evaluation time. However, the incorporation of the DCA provided a significant enhancement of the radiopacity, resulting in a good contrast between the bright CPC-treated defect and the surrounding tissues. Moreover, bone healing was observed within the untreated defect within the 8 weeks evaluation. Distributions of gray value in Figure 7b highlighted a shift of the population from gray values of 100–120 for plain CPC, to values ranging from 80 to 90 when DCA was incorporated. This effect was only detectable at the first time point, while 8 weeks postsurgery, the gray value distributions for the two cements were mostly overlapping (Fig. 7c). Gray values from untreated defects are always shown as control.

Histology and bone quantification

In none of the histological sections an adverse tissue reaction or signs of inflammation were found (Fig. 8). Both HE and EVG staining showed a uniform bone reaction in all groups. Due to decalcification of the specimens before paraffin embedding, the CPC no longer was detectable within the stained sections. Still, a round-shaped area could be recognized, which was used to localize the original defect site within the condyle. Upon light microscopical inspection, all defect areas appeared to be filled by the newly formed trabecular bone. Bone marrow-like tissue was observed in between the bone voids and the fibrotic tissue was absent. The defect location, between the cortical bone layer and the growth plates, was selected to quantify the bone tissue percentage (Fig. 9a). Eight weeks after implantation, results from the 4 experimental groups did not reveal statistically

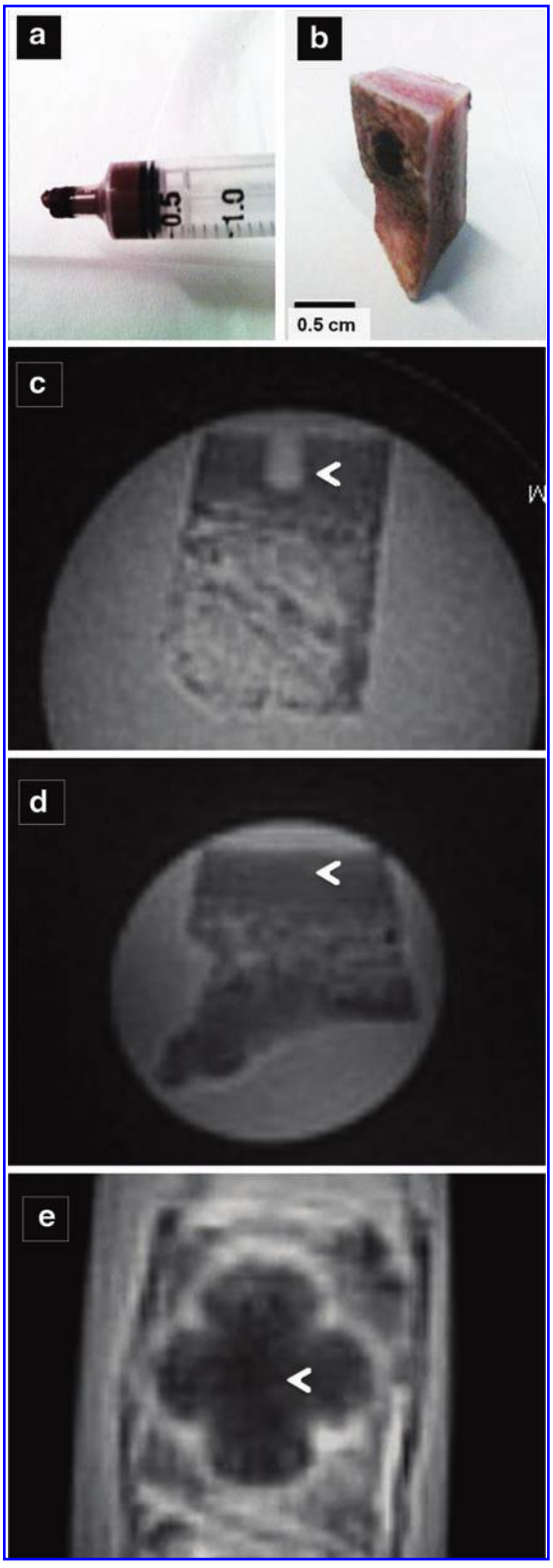

FIG. 4. *In vitro* magnetic resonance imaging (MRI). **(a)** A 5-mL syringe filled with CPC/DCA composite used to fill a bone defect created in the cortical part of ~1.5-cm^3 bone blocks **(b)**, which reveals the brownish color of the CPC. The following images are representative slides from the acquired three-dimensional (3D) dataset of the bone blocks with: **(c)** empty defect; **(d)** defect filled with plain CPC; **(e)** defect filled with CPC/DCA cement. The evident blooming effect caused by the presence of the contrast is recognizable. The bone samples were embedded in 70% ethanol. Arrows indicate the location of the defects. Color images available online at www.liebertpub.com/tec

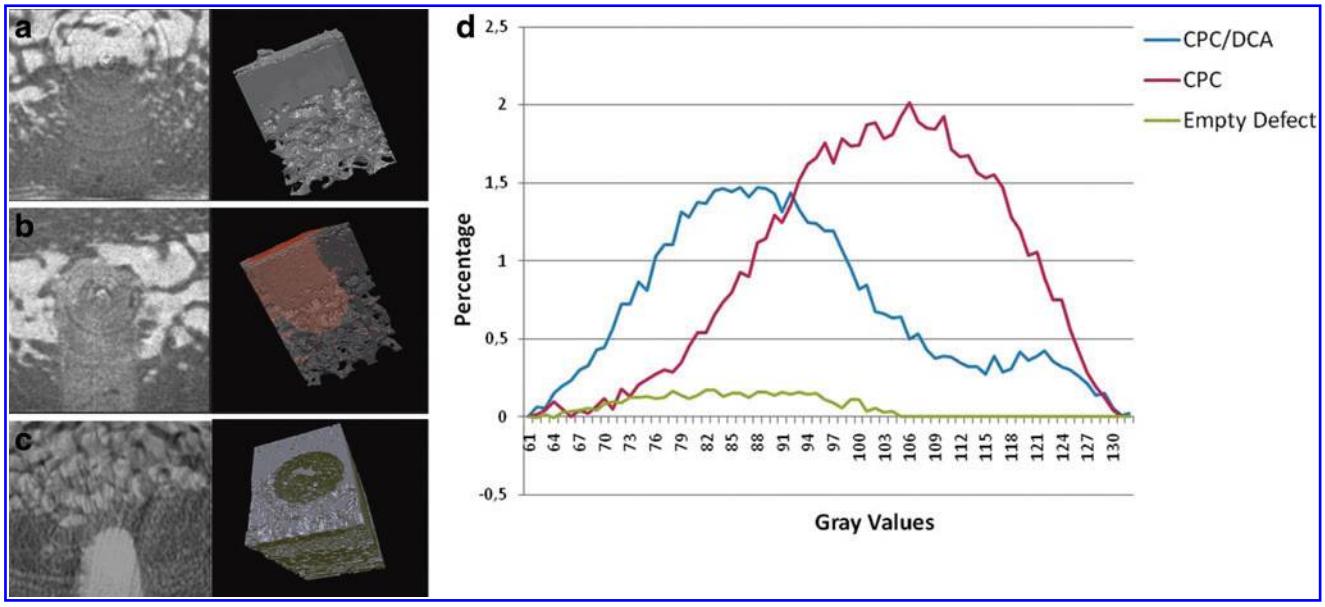

FIG. 5. *In vitro* computed tomography (CT). 2D (left panel) and 3D (right panel) μCT images of **(a)** plain CPC; **(b)** CPC/DCA cement injected into 3-mm defects in pig bone blocks; **(c)** Untreated empty defect. CPC/PLGA filling becomes clearly identifiable after incorporation of the DCA (in red in the μCT model of the whole bone block). **(d)** Gray values curve distributions for the two composite materials and the empty defect. The shift of the DCA population toward the left side of the graph is significant with $p < 0.05$.

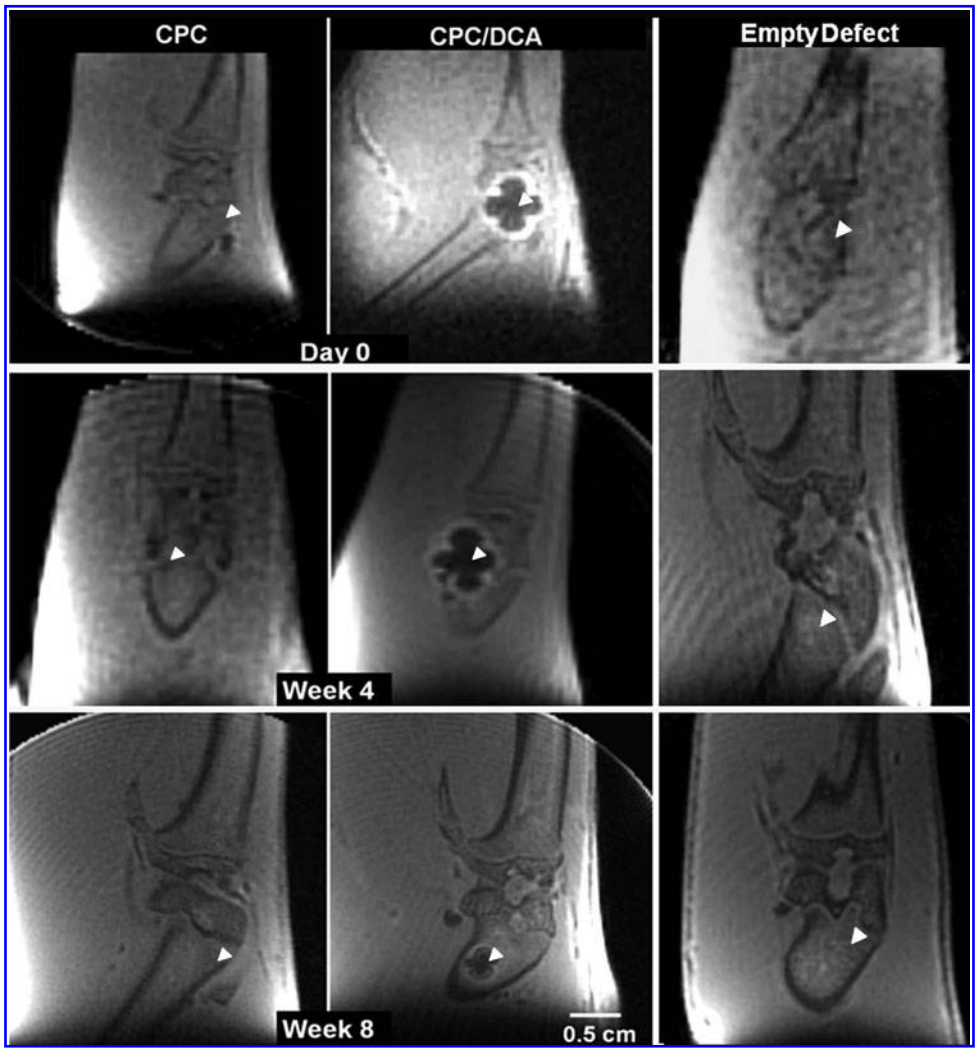

FIG. 6. *In vivo* MRI. Representative slides selected from 3D-acquired datasets of rat femoral condyle defects filled with plain CPC (first column), CPC/DCA cement (second column), or empty untreated defects (third column) acquired by Zero Echo Time sequence at day 0, 4 weeks and 8 weeks following cement installation. Arrows indicate the location of the defect.

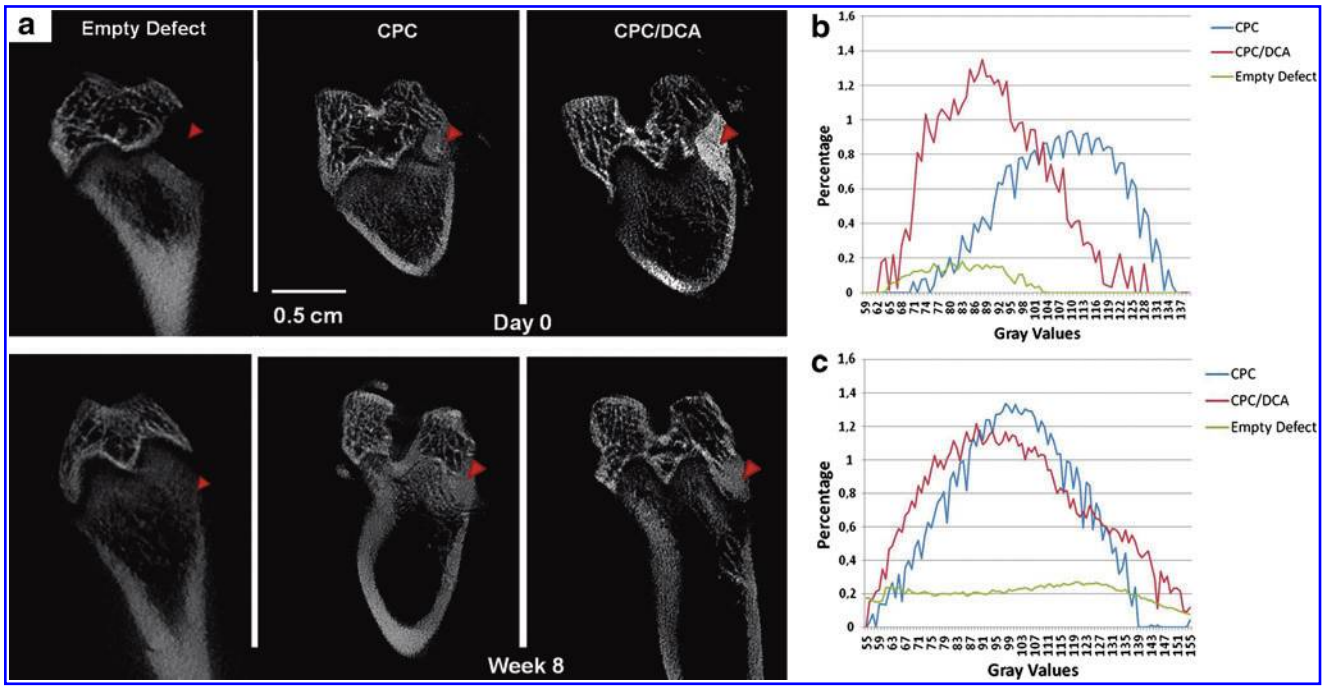

FIG. 7. *In vivo* CT. **(a)** 2D-CT images of rat femoral condyle defects filled with plain CPC, CPC/DCA cement, or empty untreated defects. Upper images were taken immediately after implantation, while bottom images were taken 8 weeks postimplantation. Red arrows indicate the defect. **(b)** Gray values curve distributions of the two composite materials at day 0. The shift of the DCA population toward the left side of the graph was considered significant with $p < 0.05$. **(c)** 8 weeks postsurgery, the differences between the two curves were no longer significant. Gray value curves from untreated defects are also shown as control.

significant differences in the bone content, which was found to be around 50% in the selected area in all groups (Fig. 9b).

Discussion

The present study aimed to test the feasibility of a DCA as an enhancer for the visualization of CPC in terms of bone contrast using CT and MR imaging. Both *in vitro* and *in vivo* assays were done. The DCA, as used, was a nanocomposite of silica beads in which two different nanoparticle types are structurally integrated. For our study, colloidal gold and superparamagnetic iron oxide nanoparticles were incorporated. The gold/iron ratio content per bead is predetermined by the detection equipment and knowledge of the individual (not dual) products already applied clinically. Following explorative pilot experiments with scans at different DCA in gradual steps from 1%–10%, it was shown that below 4% no quantifiable CT contrast was obtainable. Data also show that the higher ranges result in improper cement hardening, which is hampered. Thus, the final concentration within our cement was set at 5% wt/wt. Mixing of the two components was homogeneous conferring a uniform brown color to the cement, and indeed the cement's preparation and injection procedure did not differ from control groups. Setting time and compressive strength are of great interest to surgeons, as these data directly affect the selection of the operation procedure and postoperative care. The presence of DCA did not induce significant changes of those parameters, or even account for a slight enhancement of the mechanical strength. Thus, the handling remained acceptable within a defined range.[15,20]

The applied rat model is a well-established noncritical size femoral condyle defect to testing injectable as well as preset bone substitute materials.[21,22] The relatively uncomplicated surgical procedure, together with the easily accessible location for imaging procedures, makes this model optimal for the purposes of our study. Postimplantation imaging was evident in both techniques, which could be of great benefit to surgeons to verify proper implant placing directly postoperatively. Long-term contrast enhancement was only achievable by MRI, which signal decay over the experimental period could be assessed, thus aiding quantification of the biomaterial degradation process.

At 8 weeks after injection, CPC/DCA implants were still detectable by MRI, while CT contrast had become negligible. This indicates that also temporal degradation of the nanocomposite occurs and could allow kinetic studies with the DCA, since the contrast disappears during remodeling of the cement. The disappearance of the CT signal with time could be explained as a result of the degradation of the outer shell of the silica beads,[23,24] resulting in dilution of the gold nanoparticles. Instead, iron nanoparticles were placed on the inside of the bead, which degrade much slower. Although the location of the two embedded agents (either in the core or in the shell) does not affect directly the imaging properties of the DCA, results proved that it could become a valuable parameter when performing longitudinal studies, where a long-lasting contrast is needed. Finally, histological sections and histomorphometry proved biocompatibility and no interference of the contrast agent with the healing rate and bone ingrowth compared to plain CPC and control groups.

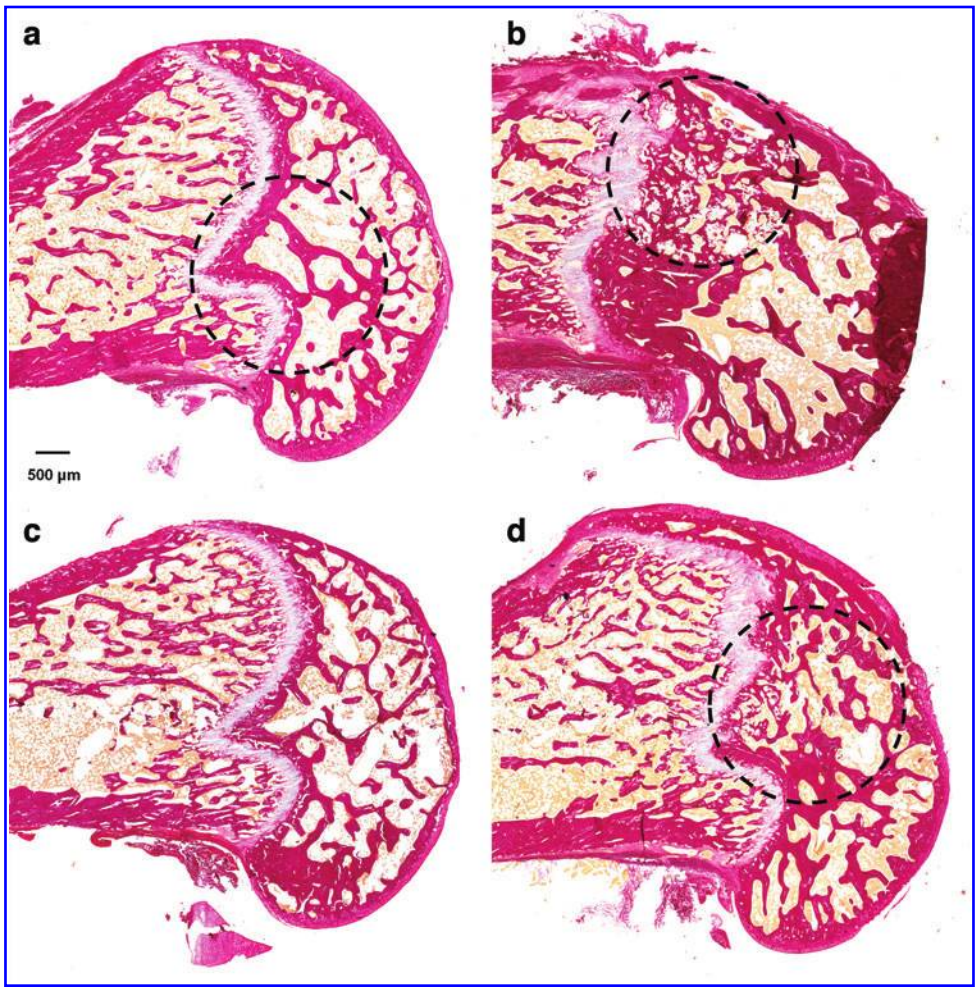

FIG. 8. Qualitative histological evaluation. Elastin van Gieson representative histological sections after 8 weeks of implantation. **(a)** Empty defect; **(b)** CPC-filled defect; **(c)** Sham-operated, no defect was created; **(d)** CPC/DCA-filled defect. A black dashed circle indicates the location of the defect. After decalcification of the samples, no traces of CPC remained visible. Color images available online at www.liebertpub.com/tec

As shown in Figure 8, the whole defect area was not located within the selected region of interest. However, the goal of the study was to test the influence of the DCA on bone growth rate and quality compared with plain CPC. Therefore, as following decalcification procedures CPC was degraded and impossible to be accurately localized, we still assume defining a well-delimited area the most accurate method. Here, the influence of the defect on bone quantity could be considered constant between all samples. Still, information regarding osteoinductive performance and degradation of CPC/DCA were precluded by the dissolution of the cement and will require further investigation.

µCT is often employed to evaluate the outcome of bone regeneration studies, as it provides qualitative as well as quantitative information based on differences in gray values between different tissues. However, visualization of CPC is still challenging and several radiopacifying materials are currently employed (bismuth, strontium, barium, colloidal gold, a.o.).[25] In a recent study by Camilleri and Gandolfi,[26] an adequate radiopacity was achieved with the use of 30% zinc oxide and similar results were obtained by the group of Húngaro Duarte[27] with zirconium oxide. However, very high concentrations of the embedded material will always (negatively) influence the handling properties of cement in

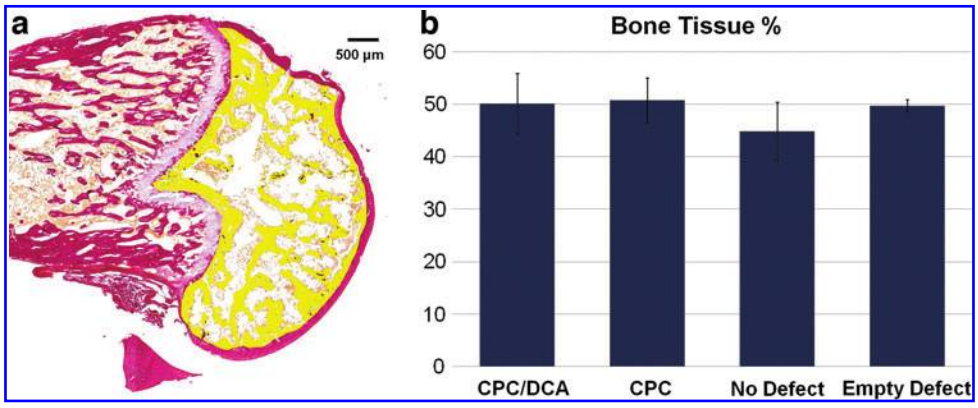

FIG. 9. Quantitative evaluation of bone formation. **(a)** Bone formation was measured within the yellow highlighted region of interest in the four experimental groups, 8 weeks after implantation. **(b)** Bone percentage in all groups was around 50%, without statistically significant differences ($p > 0.05$).

terms of setting time and mechanical outcome. A strategy to decrease the concentration of a contrast agent to avoid interferences with physicomechanical performances of the cement[28] is to choose high atomic number compounds.[11] In the study of Aguilar *et al.*,[25] bismuth oxide showed good contrast enhancing properties at a concentration of 20%, while choosing an even higher atomic mass compound as nanometric particulate of tantalum oxide, Hoekstra *et al.*[29] were able to decrease the concentration up to 10% wt/wt. Still, the problem arising from the use of such heavy metal compounds, besides unspecific reactivity, is the lack of information about their metabolic destiny, possible accumulation, and toxicity after being released after CPC degradation.[16,17,30,31] In the current study, the concentration of both radiopacifiers was set at 5% wt/wt. The structural embedding of two nanoparticles types into the silica carrier beads prevents/inhibits their release as free metal ions, and allows even the encapsulation of much higher concentrations, while avoiding the above mentioned side effects. The advantage is that after dissolution of the organic silica matrix, the inert nanoparticles can be cleared through intestinal macrophages and renal filtration.[32,33]

As a second approach, MR Imaging was selected as means of visualization. MRI is the gold standard for soft tissue imaging, such as breast and prostate, but has recently started to be exploited for hard tissue applications too. The development of short Echo Time acquisition sequences, like Ultra Short Echo Time and ZTE,[8–10,34] opened the way to new possibilities for bone-related applications.

In a recent study, Sun *et al.*[35] aimed to evaluate the feasibility of ZTE acquisition for CPC visualization. Gd-DTPA (Magnevist®) and USPIO (Sinerem®) were used as *in vitro* and *in vivo* enhancers of CPC contrast. Despite the positive results in terms of contrast enhancement, both compounds negatively affected the physical and mechanical properties of CPC, even at concentrations as low as 1% wt/wt. This precludes their further clinical application. The herein proposed Dual Contrast approach allows, by encapsulation and isolation of the contrast agents, to prevent unspecific reactivity. The CT acquisition could be directly translated into clinical applications; however, MR bone imaging is still undergoing developmental and optimization steps at a preclinical level. Although ZTE acquisition represents a valuable tool for hard tissue imaging, the integration within clinical instruments is still an ongoing process as first specific instrumental as well as software requirements must be fulfilled.

In the present study, SPIO particles and colloidal gold nanoparticles were jointly encapsulated into the silica beads. Although gadolinium-chelates[36,37] have been described earlier, SPIO currently appear to be preferred as MRI contrast agents. Such particle labeling is considered favorable because: (1) SPIO account for the highest change in signal per unit of metal, in particular, on T2*-weighted images. Since SPIO are composed of thousands of iron atoms, they defeat the inherent low-contrast agent sensitivity of MRI; (2) SPIO are biocompatible and biodegradable and can be reused/recycled by cells using normal biochemical pathways for iron metabolism; (3) SPIO can be magnetically manipulated, while their magnetic properties differ according to size, as well as their structural conformation (e.g., free vs. bound state).[38]

Gold nanoparticles have been shown to be superior compared to several other radiopacifiers (e.g., Iodinated compounds). The application of Gold results in higher absorption with less bone and tissue interference achieving better contrast with lower X-ray dose.[39] In fact, imaging gold at 80–100 keV reduces interference from bone absorption and takes advantage of lower soft tissue absorption helping to reduce patient radiation doses.[40]

The encapsulation of both compounds into a silica matrix appeared to be a good strategy to prevent side reactions between CPC and contrast agents. A major drawback of iron oxide particles as an MR-T2* contrast enhancer is the resulting so-called blooming effect, often caused by overload or simple clustering of iron oxide particles within the tissue.[41]

Possible strategies to reduce the blooming effect are suggested by recent studies and consist in reducing the concentration of nanoparticles, in the tuning and modification of the MR acquisition parameters,[42,43] or incorporation of MR contrast agents, like gadolinium or fluorine. Moreover, MRI contrast agents are usually employed in Gradient Echo scans at 1.5 Tesla in which blooming effects are less evident. Despite, what needs to be taken in consideration is that the effect of the contrast agents also strongly depends on the MRI technique employed. In our case, in contrast with Gradient Echo techniques, with the ZTE, the affected signal is not lost, but blurred as well as dislocated, contributing to a further signal intensity increase. The localization of our CPC/DCA resulted, therefore, more obvious, but at the same time, a direct signal quantification was hampered. Still, recent literature has already shown that quantification of the iron particle-signal is possible by means of novel susceptibility mapping techniques in combination with relaxation time mapping techniques. However, these methods have to be developed further, as only preliminary studies are currently reported.[44,45]

The hereby presented formulation allowed the clear verification of proper implant placing with both methods. The long-term contrast enhancement provided by MRI opens longitudinal quantification possibilities. The contrast degradation, proved by disappearance of CT contrast enhancement, suggested that degradation analyses would also be possible and tailoring degradation and contrast persistance is a way that will be surely explored in future studies.

Furthermore, due to the inhert behavior of the carrier, we assume that the DCA could be incorporated within virtually any kind of material, that is, different ceramic or polymer-based materials. Finally, we envision that besides contrast-enhancing agents, the hereby proposed bead-carrier can ideally also be employed for the incapsulation of different molecules (i.e., bioactive molecules, drugs, growth factors, etc.) for regenerative medicine applications. In conclusion, the combination of two different contrast agents within one silica bead carrier product allows to obtain complementary information from multiple imaging modalities, without changing the overall biomaterial performance in calcium phosphate ceramic.

Acknowledgments

The authors would like to thank Natasja van Dijk, Vincent Cuijpers, Martijn Martens, Bianca Lemmers–van de Weem,

and Kitty Lemmens–Hermans for their technical assistance. SEM was performed at the microscope imaging centre (MIC) of the Nijmegen Centre for Molecular Life Sciences (NCMLS). The research leading to these results has received funding from the European Community's Seventh Framework Programme (MultiTERM, grant agreement nr 238551).

Disclosure Statement

No competing financial interests exist.

References

1. Tanner, E. Orthopedics to take center stage in coming decade. Medmonitor Special Millennio Edition-Datamonitor, 2000. The need for bone substitutes, http://www.btec.cmu.edu/reFramed/tutorial/boneSubs/boneSubs.html
2. Klijn, R.J., van den Beucken, J.J., Félix Lanao, R.P., Veldhuis, G., Leeuwenburgh, S.C., Wolke, J.G., Meijer, G.J., and Jansen, J.A. Three different strategies to obtain porous calcium phosphate cements: comparison of performance in a rat skull bone augmentation model. Tissue Eng Part A. **18,** 1171, 2012.
3. Félix Lanao, R.P., Hoekstra, J.W., Wolke, J.G., Leewenburgh, S.C., Plachokova, A.S., Boerman, O.C., van de Beucken, J.J., and Jansen, J.A. Porous calcium phosphate cement for alveolar bone regeneration. J Tissue Eng Regen Med 2012 [Epub ahead of print]; DOI: 10.1002/term.1546.
4. Hoekstra, J.W., Klijn, R.J., Meijer, G.J., van den Beucken, J.J., and Jansen, J.A. Maxillary sinus floor augmentation with injectable calcium phosphate cements: a pre-clinical study in sheep. Clin Oral Implants Res 2012 [Epub ahead of print]; DOI: 10.1111/j.1600-0501.2012.02421.x.
5. van de Watering, F.C., van den Beucken, J.J., Walboomers, X.F., and Jansen, J.A. Calcium phosphate/poly(D,L-lactic-co-glycolic acid) composite bone substitute materials: evaluation of temporal degradation and bone ingrowth in a rat critical-sized cranial defect. Clin Oral Implants Res **23,** 151, 2012.
6. Du, J., Bydder, M., Takahashi, A.M., Carl, M., Chung, C.B., and Bydder, G.M. Short T2 contrast with three-dimensional ultrashort echo time imaging. Magn Reson Imaging **29,** 470, 2011.
7. Anumula, S., Wehrli, S.L., Magland, J., Wright, A.C., and Wehrli, F.W. Ultra-short echo-time MRI detects changes in bone mineralization and water content in OVX rat bone in response to alendronate treatment. Bone **46,** 1391, 2010.
8. Weiger, M., Pruessmann, K.P., and Hennel, F. MRI with zero echo time: hard versus sweep pulse excitation. Magn Reson Med **66,** 379, 2011.
9. Beaman, F.D., Bancroft, L.W., Peterson, J.J., Kransdorf, M.J., Menke, D.M., and DeOrio, J.K. Imaging characteristics of bone graft materials. Radiographics **26,** 373, 2006.
10. Ginebra, M.P., Albuixech, L., Fernandez-Barragan, E., Aparicio, C., Gil, F.J., San, R.J., Vazquez, B., and Planell, J.A. Mechanical performance of acrylic bone cements containing different radiopacifying agents. Biomaterials **23,** 1873, 2002.
11. Baroth, S., Bourges, X., Fellah, B.H., and Daculsi, G. Radiopaque strategy for bone injectable substitute. Key Eng Mater **39,** 361, 2008.
12. Chan, D.C., Titus, H.W., Chung, K.H., Dixon, H., Wellinghoff, S.T., and Rawls H.R. Radiopacity of tantalum oxide nanoparticle filled resins. Dent Mater **15,** 219, 1999.
13. Wang, X., Ye, J., and Wang, Y. Influence of a novel radiopacifier on the properties of an injectable calcium phosphate cement. Acta Biomater **3,** 757, 2007.
14. Barbier, O., Jacquillet, G., Tauc, M., Cougnon, M., and Poujeol, P. Effect of heavy metals on, and handling by, the kidney. Nephron Physiol **99,** 105, 2005.
15. Sharma, S.K., Goloubinoff, P., and Christen, P. Heavy metal ions are potent inhibitors of protein folding. Biochem Biophys Res Commun **25,** 372, 2008.
16. Matson, M.L., and Wilson, L.J. Nanotechnology and MRI contrast enhancement. Future Med Chem **2,** 491, 2010.
17. Sonvico, F., Dubernet, C., Colombo, P., and Couvreur, P. Metallic colloid nanotechnology, applications in diagnosis and therapeutics. Curr Pharm Des **11,** 2095, 2005.
18. Lopez-Heredia, M.A., Sariibrahimoglu, K., Yang, W., Bohner, M., Yamashita, D., Kunstar, A., van Apeldoorn, A.A., Bronkhorst, E.M., Félix Lanao, R.P., Leeuwenburgh, S.C., Itatani, K., Yang, F., Salmon, P., Wolke, J.G., and Jansen, J.A. Influence of the pore generator on the evolution of the mechanical properties and the porosity and interconnectivity of a calcium phosphate cement. Acta Biomater **8,** 404, 2012.
19. Stober, W., Fink, A., and Bohn, E. Controlled growth of monodisperse silica spheres in micron size range. J Colloid Interface Sci **26,** 62, 1968.
20. Chen, D.M., and Fu, Y.F. Evaluation on the mechanical properties of the solid solution of strontium substituted hydroxyapatite. Chin J Stoma **19,** 178, 2001.
21. Schouten, C., van den Beucken, J.J., de Jonge, L.T., Bronkhorst, E.M., Meijer, G.J., Spauwen, P.H., and Jansen, J.A. The effect of alkaline phosphatase coated onto titanium alloys on bone responses in rats. Biomaterials **30,** 6407, 2009.
22. Castellani, C., Zanoni, G., Tangl, S., van Griensven, M., and Redl, H. Biphasic calcium phosphate ceramics in small bone defects: potential influence of carrier substances and bone marrow on bone regeneration. Clin Oral Implants Res **20,** 1367, 2009.
23. Kursawe, M., Glaubitt, W., and Thierauf, A. Biodegradable silica fibers from sols. J Sol-Gel Sci Technol **13,** 267, 1998.
24. Lauwers, A.M., and Heinen, W. Bio-degradation and utilization of silica and quartz. Arch Microbiol **95,** 67, 1974.
25. Aguilar, F.G., Garcia Lda, F., Rossetto, H.L., Pardini, L.C., and Pires-de-Souza Fde, C. Radiopacity evaluation of calcium aluminate cement containing different radiopacifying agents. J Endod **37,** 67, 2011.
26. Camilleri, J., and Gandolfi, M.G. Evaluation of the radiopacity of calcium silicate cements containing different radiopacifiers. Int Endod J **43,** 21, 2010.
27. Húngaro Duarte, M.A., de Oliveira El Kadre, G.D., Vivan, R.R., Guerreiro Tanomaru, J.M., Tanomaru Filho, M., and de Moraes, I.G. Radiopacity of Portland cement associated with different radiopacifying agents. J Endod **35,** 737, 2009.
28. Camilleri, J. Evaluation of the physical properties of an endodontic Portland cement incorporating alternative radiopacifiers used as root-end filling material. Int Endod J **43,** 231, 2010.
29. Hoekstra, J.W., van den Beucken, J.J., Leeuwenburgh, S.C., Meijer, G.J., and Jansen, J.A. Tantalumpentoxide as a radiopacifier in injectable calcium phosphate cements for bone substitution. Tissue Eng Part C Methods **17,** 907, 2011.
30. Chowdhury, B.A., and Chandra, R.K. Biological and health implications of toxic heavy metal and essential trace element interactions. Prog Food Nutr Sci **11,** 55, 1987.
31. Lavery, T.J., Kemper, C.M., Sanderson, K., Schultz, C.G., Coyle, P., Mitchell, J.G., and Seuront, L. Heavy metal toxicity of kidney and bone tissues in South Australian adult bottlenose dolphins (Tursiops aduncus). Mar Environ Res **67,** 1, 2009.

32. Sato, K., Yokosuka, S., Takigami, Y., Hirakuri, K., Fujioka, K., Manome, Y., Sukegawa, H., Iwai, H., and Fukata, N. Size-tunable silicon/iron oxide hybrid nanoparticles with fluorescence, superparamagnetism and biocompatibility. J Am Chem Soc **133,** 18626, 2011.
33. Choi, H.S., Liu, W., Misra, P., Tanaka, E., Zimmer, J.P., Itty Ipe, B., Bawendi, M.G., and Frangioni, J.V. Renal clearance of quantum dots. Nat Biotechnol **25,** 1165, 2007.
34. Gatehouse, P.D., and Bydder, G.M. Magnetic resonance imaging of short T2 components in tissue. Clin Radiol **58,** 1, 2003.
35. Sun, Y., Ventura, M., Oosterwijk, E., Jansen, J.A., Walboomers, X.F., and Heerschap, A. Zero echo time (ZTE) MR imaging of contrast-agent-enhanced calcium phosphate bone defect fillers. Tissue Eng Part C: Methods 2012 [Epub ahead of print]; DOI: 10.1089/ten.TEC.2011.0745.
36. Olsson, M., Persson, B., Salford, L., and Schroder, U. Ferromagnetic particles as contrast agents in T2 NMR imaging. Magn Reson Imaging **4,** 437, 1986.
37. Renshaw, P.F., Owen, C.S., McLaughlin, A.C., Frey, T.G., and Leight, J.S., Jr. Ferromagnetic contrast agents: a new approach. Magn Reson Med **3,** 217, 1986.
38. Bulte, J.W.M., and Kraitchman, D.L. Iron oxide MR contrast agents for molecular and cellular imaging. NMR Biomed **17,** 484, 2004.
39. Atkins, H.L., Fairchild, R.G., Robertson, J.S., and Greenberg, D. Effect of absorption edge filters on diagnostic x-ray spectra. Radiology **115,** 431, 1975.
40. Hainfeld, J.F., Slatkin, D.N., Focella, T.M., and Smiliwits, H.M. Gold nanoparticles: a new X-ray contrast agent. Br J Radiol **79,** 248, 2006.
41. Brekke, C., Williams, S.C., Price, J., Thorsen, F., and Modo, M. Cellular multiparametric MRI of neural stem cell therapy in a rat glioma model. Neuroimage **37,** 769, 2007.
42. Thu, M.S., Najbauer, J., Kendall, S.E., Harutyunyan, I., Sangalang, N., Gutova, M., Metz, M.Z., Garcia, E., Frank, R.T., Kim, S.U., Moats, R.A., and Aboody, K.S. Iron labeling and pre-clinical MRI visualization of therapeutic human neural stem cells in a murine glioma model. PLoS One **29,** 7218, 2009.
43. Tang, T.Y., Muller, K.H., Graves, M.J., Li, Z.Y., Walsh, S.R., Young, V., Sadat, U., Howarth, S.P.S., and Gillard, J.H. Iron oxide particles for atheroma imaging. Arterioscler Thromb Vasc Biol **29,** 1001, 2009.
44. Girard, O.M., Ramirez, R., McCarty, S., and Mattrey, R.F. Toward absolute quantification of iron oxide nanoparticles as well as cell internalized fraction using multiparametric MRI. Contrast Media Mol Imaging **7,** 411, 2012.
45. Girard, O.M., Du, J., Agemy, L., Sugahara, K.N., Kotamraju, V.R., Ruoslahti, E., Bydder, G.M., and Mattrey, R.F. Optimization of iron oxide nanoparticle detection using ultrashort echo time pulse sequences: comparison of T1, T2*, and synergistic T1-T2* contrast mechanisms. Magn Reson Med **65,** 1649, 2011.

Address correspondence to:
John A. Jansen, DDS, PhD
Department of Biomaterials
Radboud University Nijmegen Medical Center
THK 309
P.O. Box 9101
6500 HB Nijmegen
The Netherlands

E-mail: j.jansen@dent.umcn.nl

Received: January 8, 2012
Accepted: October 17, 2012
Online Publication Date: December 21, 2012